ORIGINAL RESEARCH ARTICLE

Dynamic Grain Growth Driven by Subgrain Boundaries in an Interstitial-Free Steel During Deformation at 850 °C

THOMAS J. BENNETT IV and ERIC M. TALEFF

A mechanism is proposed for dynamic grain growth (DGG) by subgrain boundaries driving grain-boundary migration. This mechanism is evaluated against data from an interstitial-free steel tested in tension at 850 °C and a true-strain rate of 10^{-4} s^{-1} and rapidly quenched to preserve microstructures evolved during deformation. Tensile tests produced steady-state flow, distinct subgrains, and rapid DGG. Static annealing alone produced static grain growth (SGG) that was much slower than DGG. Electron backscatter diffraction (EBSD) provided grain size and orientation measurements. High-resolution electron backscatter diffraction (HR-EBSD) was used to accurately measure subgrain sizes and subgrain boundary misorientations. The average grain size increased linearly with strain during DGG, but the average subgrain size remained constant during straining. The average subgrain boundary misorientation increased with strain, initially rapidly and then slowly. The dihedral angle imposed in grain boundaries by intersecting subgrain boundaries decreased with increasing subgrain boundary misorientation, which supports the proposed mechanism for DGG. The driving pressure for grain-boundary migration from subgrain boundaries is estimated to be approximately one order in magnitude greater than that from dislocation density reduction under the conditions examined.

https://doi.org/10.1007/s11661-023-07256-w

I. INTRODUCTION

GRAIN growth is the gradual increase of average grain size in a recrystallized material.[1] This study investigates how the subgrains developed in a recrystallized interstitial-free steel during steady-state deformation at elevated temperature influence dynamic grain growth, that is grain growth during plastic deformation. It is fundamentally concerned with how subgrain boundaries may interact with high-angle grain boundaries to drive grain-boundary migration and, thus, grain growth during deformation. Grain-boundary migration is of great practical importance to controlling grain size in metals and their alloys during thermo-mechanical processing. Plastic deformation at elevated temperature can dramatically affect the rates of grain-boundary migration and grain growth.[2–18] Grain growth that occurs at elevated temperature during concurrent plastic deformation is termed *dynamic* grain growth (DGG). By contrast, grain growth that occurs during static annealing without concurrent deformation is termed *static* grain growth (SGG). DGG phenomena are important to understanding microstructural evolution and material behavior during thermo-mechanical processing and elevated temperature service when creep deformation may occur.

Grain growth can be further classified as either *normal* or *abnormal* based upon the relative growth rates among grains. Normal grain growth is characterized by a continuous uniform coarsening of the microstructure during which the initial grain size distribution, typically log-normal, shifts upwards over time without changing its essential shape.[1,19] Abnormal grain growth is characterized by the rapid and often discontinuous growth of one or a few grains to sizes significantly larger than those of grains in the surrounding microstructure.[1,19] Abnormal grain growth can cause an initially unimodal grain size distribution to become bimodal.[19] Combining these two classification schemes leads to four categories of grain growth: 1. static normal grain growth, 2. static abnormal grain growth, 3. dynamic normal grain growth, and 4. dynamic abnormal grain growth.[18] The present investigation is concerned with static and dynamic normal grain growth phenomena.

SGG theory has been treated extensively in the literature, and current understanding is summarized in modern textbooks.[19,20] The driving pressures for

THOMAS J. BENNETT IV and ERIC M. TALEFF are with the Department of Mechanical Engineering, University of Texas at Austin, 204 East Dean Keeton St., Stop C2200, Austin, 78712, TX. Contact e-mail: thomas.bennett@utexas.edu
Manuscript submitted July 3, 2023; accepted November 7, 2023.
Article published online December 12, 2023

boundary migration classically considered of greatest practical importance are those from grain boundary curvature and the elimination of stored deformation energy, synonymous in theory with the elimination of dislocation density. These driving pressures have been applied to explain many aspects of SGG[20] but are not always consistent with experimental observations. For example, recent investigations of grain growth in Ni by Bhattacharya *et al.* identified no correlation between grain boundary velocities and boundary curvatures, a result that calls aspects of classical theory into question.[21]

DGG has received much less attention than SGG. DGG has been observed in creep tests[22] and superplastic deformation.[2–7] DGG during superplastic deformation has been attributed to effects from grain boundary sliding, such as excess vacancies near grain boundaries[2,3] and damage at triple junctions.[4] Rabinovich and Trifonov[5] proposed that geometrical effects from grain elongation during superplastic deformation are significant to DGG. These proposed mechanisms are not applicable to DGG when superplastic deformation mechanisms are not active. Bate and Hyde[7,8] investigated dynamic normal grain growth in superplastic and non-superplastic Al alloys and proposed that deformation disrupts Zener pinning effects, accelerating grain-boundary migration. Bate incorporated a model for this effect into numerical simulations of DGG.[23] Onuki *et al.*[24] investigated dynamic normal grain growth in Fe-3Si (mass pct) under plane-strain compression and suggested that grains preferred for growth are those oriented for low Taylor factors and stability against deformation. Rupp *et al.*[18] investigated dynamic normal grain growth in a titanium-added interstitial-free steel and observed the dynamic growth of grains oriented for high Taylor factors, which contrasts with the results of Onuki *et al.* Among the most dramatic examples of DGG are the observations of dynamic abnormal grain growth in the body-centered cubic (BCC) refractory metals Mo and Ta,[10–17] which include the production of Mo single crystals several centimeters in length.[12] Microstructural investigations of dynamic abnormal grains produced in Mo suggested that subgrains may play an important role in dynamic grain growth.[17] A mechanism by which subgrain boundaries intersecting high-angle grain boundaries provide a driving force for boundary migration was suggested by Noell and Taleff based upon those observations.[17] The details and feasibility of this mechanism are explored in the present study.

For BCC metals and face-centered cubic (FCC) metals of high-stacking-fault energy, creep deformation typically produces well-defined subgrains.[25–31] Subgrains are regions of approximately constant crystallographic orientation within deformed grains. Subgrains are separated by distinct low-angle boundaries, termed subgrain boundaries, with misorientations ranging from a small fraction of a degree to several degrees. Subgrains fully develop as primary creep transitions into steady state, where subgrain diameter is inversely proportional to stress.[25–28] Figure 1 presents the microstructure of a titanium-added interstitial-free steel that exhibits subgrains from high-temperature deformation. This microstructure was produced by tensile elongation at 850 °C in the steady-state creep regime and was preserved for subsequent characterization by rapidly quenching the specimen while holding stress steady.

The present study investigates the role of subgrains in driving DGG in the same titanium-added interstitial-free (Ti-IF) steel sheet material that provided Figure 1. DGG was induced following recrystallization in a series of tensile tests at 850 °C. SGG was similarly induced in a series of annealing heat treatments at the same temperature. The resulting microstructures were characterized using scanning electron microscopy (SEM) techniques, principally electron backscatter diffraction (EBSD). Subgrain boundaries can have misorientation angles on the order of 0.1 deg, smaller than the typical limits of resolution for standard EBSD indexing methods based on the Hough transform. High-resolution electron backscatter diffraction (HR-EBSD), which provides a relative orientation resolution sufficient to resolve boundary misorientations as low as 0.1 deg, was, therefore, utilized for subgrain characterization. The data produced are used to evaluate the effect of subgrain boundaries on DGG by interpretation through theory, which is presented next.

II. THEORY

The Einstein relation from kinetic theory embodies the hypothesis of a mobility defined as the drift velocity divided by a driving force.[32–34] This concept of mobility has been fundamental to understanding migration phenomena in force-producing fields. Many theories of grain-boundary migration borrow this concept to define the velocity of boundary migration, v, as the product of boundary mobility, m, and a driving force described by thermodynamic pressure P on the boundary such that[20]

$$v = mP. \qquad [1]$$

This approach inherently assumes that a continuum field theory reasonably approximates the physics of grain-boundary migration. The case of elastic stress and strain fields obviously fits this approach well for many examples of practical interest.[20,35–39] The influence of plastic deformation on grain-boundary migration has been addressed similarly by approximating dislocation density, ρ, as a continuum field describing stored deformation energy from plastic straining.[20] The appropriateness of this assumption clearly depends on length scale. Eliminating dislocation density, and its associated stored deformation energy, reduces total energy. Approximating the energy per unit length of a dislocation line as $\mu b^2/2$, where μ is the elastic shear modulus and b is the magnitude of the Burgers vector, produces the usual estimate for the thermodynamic driving pressure on a grain boundary to eliminate dislocation density by migration,[20]

$$P_{\mathrm{d}} = \frac{1}{2}\,\rho\mu b^2. \qquad [2]$$

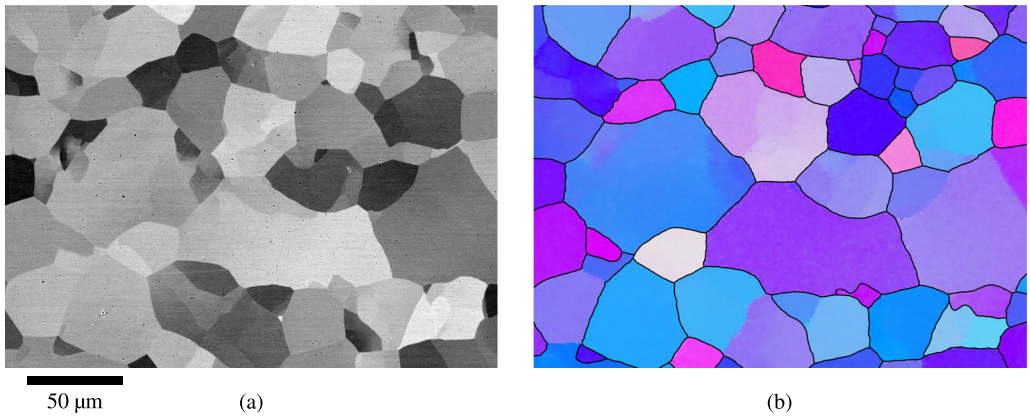

Fig. 1—(*a*) The microstructure in Ti-IF steel after deformation to $\epsilon_f = 0.225$ at $\dot{\epsilon} = 10^{-4}$ s^{-1} and 850 °C is shown in a backscattered electron image. (*b*) EBSD data from the same region as (a) are presented as an inverse pole figure (IPF) map; the color key is the same as that shown in Fig. 6. Solid lines indicate grain boundaries with a misorientation greater than five degrees. Subgrain boundaries in (a) are identifiable upon comparison with (b). Both images are presented at the same scale (Color images are available online).

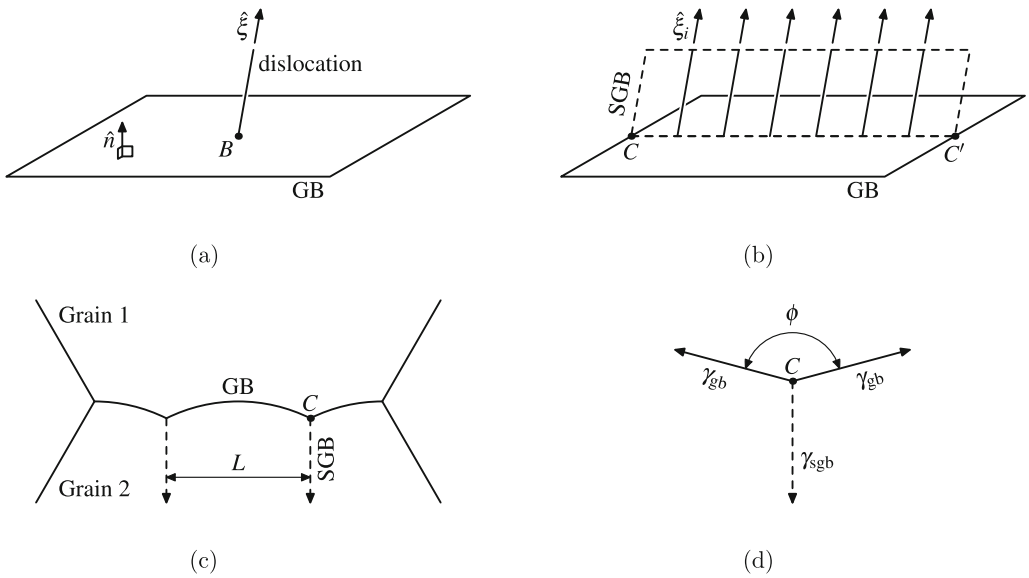

Fig. 2—(*a*) A single dislocation line intersects a high-angle grain boundary (GB) at point *B*. (*b*) A planar array of dislocations forming a subgrain boundary (SGB) intersects a high-angle grain boundary (GB) along line $\overline{CC'}$. (*c*) Subgrain boundaries spaced a distance *L* apart intersect a high-angle grain boundary (GB), producing local curvature near the lines of intersection. (*d*) The balance of forces between the high-angle grain boundary and subgrain boundary at *C* creates the dihedral angle ϕ.

This theoretical approach raises a question of information passing. Thermodynamics dictates that the grain boundary will migrate toward the highest dislocation density to produce the greatest energy reduction. But, how does the grain boundary know that direction? The continuum field theory for dislocation density assumes that the grain boundary can sense this direction through gradients in dislocation density field intensity. However, it is not always reasonable to model dislocation density as a continuous field. The approach suggested by Eq. [2] must be questioned at small length scales or whenever dislocation density might be discontinuous. Fortunately, these issues can be overcome by considering discrete dislocations.

Consider a nominally planar high-angle grain boundary defined by the unit normal vector $\hat{n}$ shown in Figure 2(a). This grain boundary is intersected at point *B* by a straight dislocation line with unit sense vector $\hat{\xi}$. The dislocation terminates at point *B* and creates there a force on the grain boundary. Here, $\hat{\xi}$ is taken as pointing away from *B*. The force on the boundary at *B* may be approximated using the elastic strain energy per unit dislocation line length, which is equivalent to a line tension,

$$\mathbf{f} = \alpha \mu b^2 \hat{\xi}\,, \qquad [3]$$

where α is a constant that depends on dislocation character and elastic properties[40–42] and is typically in the range of $\alpha = 0.5$ to 1.0.[42] This force encourages

boundary migration along the dislocation line direction $\hat{\xi}$. Considering this discrete dislocation makes clear that the force for migration of a boundary is communicated directly by the dislocations that intersect that boundary, whether the distribution of dislocations is inhomogeneous or sufficiently homogeneous to merit the assumption of a continuous dislocation density field.

The action from N dislocations intersecting area A on one side of a high-angle grain boundary might be generalized for relatively homogeneous dislocation distributions by defining the dislocation density as $\rho = N/A$. To determine the driving pressure that acts normally to the grain boundary, the component of force normal to that boundary from each dislocation i can be calculated from Eq. [3] as follows:

$$f_{n,i} = \alpha_i \mu b^2 \left(\hat{\xi}_i \cdot \hat{n} \right). \quad [4]$$

Summing the contributions from the N dislocations intersecting the boundary area A produces a driving pressure,

$$\begin{aligned} P_{\mathrm{d}} &= \frac{1}{A} \sum_{i=1}^{N} f_{n,i} \\ &= \frac{\rho \mu b^2}{N} \sum_{i=1}^{N} \alpha_i \left(\hat{\xi}_i \cdot \hat{n} \right), \\ &= \bar{\alpha} \rho \mu b^2 \end{aligned} \quad [5]$$

where $\bar{\alpha}$ is an average value produced by the summation. If $\bar{\alpha} \approx 1/2$, then this result is the same as that from the classical field theory that produced Eq. [2]. As expected, these two theoretical approaches produce equivalent results when it is reasonable to model dislocation density as a continuous field.

Dislocation substructures arrange into low-angle boundaries that form subgrains during the high-temperature deformation of pure metals and Class II (also called Class M) alloys with high stacking-fault energies.[26,27,43,44] Examine how these subgrain boundaries may interact with high-angle grain boundaries using Figure 2(b). Consider first a simple planar array of identical dislocations, as shown in Figure 2(b), that produces a low-angle subgrain boundary (SGB) intersecting a high-angle grain boundary (GB) along line $\overline{CC'}$. Equation [5] could be used to calculate the resulting migration pressure on the grain boundary, but the forces from the individual dislocations can be also approximated as a line of force acting along $\overline{CC'}$. That line force is equivalent to the subgrain boundary energy, γ_{sgb}. Consider now the more realistic case of a high-angle grain boundary between two grains, labeled as Grain 1 and Grain 2 in Figure 2(c). Grain 1 is free of subgrains, but Grain 2 contains subgrain boundaries spaced a length L apart and intersecting a high-angle grain boundary (GB) with Grain 1. Note that the distance L is related to the subgrain size, λ. The intersection line $\overline{CC'}$ in Figure 2(b) would be perpendicular to the figure in (c). At each line of intersection, the subgrain boundaries produce a line force on the high-angle grain boundary, causing local curvature. Together, the subgrain boundary intersections produce forces that can be approximated as an average downward driving pressure for migration on the high-angle grain boundary,

$$P_{\mathrm{sgb}} = \frac{\gamma_{\mathrm{sgb}}}{L}. \quad [6]$$

For the case of subgrains in both Grain 1 and Grain 2, the downward driving pressure for migration would be determined by the difference in subgrain characteristics on the two sides of the grain boundary as,

$$\Delta P_{\mathrm{sgb}} = \frac{\gamma_{\mathrm{sgb},2}}{L_2} - \frac{\gamma_{\mathrm{sgb},1}}{L_1}. \quad [7]$$

By this analysis, subgrains developed during high-temperature deformation produce a driving pressure for the migration of high-angle grain boundaries, which could accelerate grain growth. Furthermore, high-angle grain boundaries should migrate into grains containing the smallest subgrains with the highest subgrain boundary energies.

The boundary intersection at location C in Figure 2(c) is examined closely in Figure 2(d). The subgrain boundary produces a dihedral angle ϕ in the high-angle grain boundary, and this angle depends on the energies of the two boundary types as,

$$\cos\left(\frac{\phi}{2}\right) = \frac{1}{2} \frac{\gamma_{\mathrm{sgb}}}{\gamma_{\mathrm{gb}}}, \quad [8]$$

where γ_{gb} is the energy of the high-angle grain boundary. The energy of a boundary produced by a planar array of dislocations was considered by Shockley and Read,[45,46] who determined that the boundary energy is governed by the misorientation angle, θ, across the boundary. The resulting Read-Shockley equation is generally considered accurate for low-angle boundaries.[41] Applying this to the case of subgrain boundaries provides,

$$\gamma_{\mathrm{sgb}} = \gamma_0 \, \theta \, (A_{\mathrm{RS}} - \ln \theta), \quad [9]$$

where γ_0 and A_{RS} are constant parameters. Equations [8] and [9] combine to predict dihedral angle as a function of subgrain boundary misorientation angle. This prediction can be tested against experiment and used to calculate the driving pressure from subgrains for the migration of high-angle grain boundaries.

III. EXPERIMENTAL PROCEDURES

A commercial Ti-IF steel sheet material, provided by I/N Tek (New Carlisle, IN) with a thickness of 0.69 mm, was tested to investigate the influence of subgrains on DGG. The Ti-IF steel composition, as reported by the manufacturer, is provided in Table I. The sheet material was received in a hard as-rolled condition. This is the same material previously investigated by Rupp *et al.*[18] Two types of tests were

Table I. Ti-IF Steel Composition in Wt Pct

Mn	Al	Ti	Cr	Cu	Ni	S	P	Nb	Si	Mo
0.1319	0.065	0.0428	0.0294	0.0188	0.0185	0.0118	0.0112	0.0097	0.0049	0.004

As	N	C	Pb	Sn	V	Sb	B	Ca	Fe
0.0034	0.00248	0.0024	0.001	0.001	0.001	0.0007	0.0001	0.0001	bal.

Table II. Test Conditions Include Time at Temperature (t), Final True Strain (ϵ_f), and True-Strain Rate ($\dot{\epsilon}$)

Test Type	t (h)	ϵ_f	$\dot{\epsilon}$ (s^{-1})
Static	1.00	0	0
Static	2.58	0	0
Static	4.92	0	0
Static	8.00	0	0
Dynamic	1.28	0.076	10^{-4}
Dynamic	1.28	0.086	10^{-4}
Dynamic	1.33	0.101	10^{-4}
Dynamic	1.39	0.124	10^{-4}
Dynamic	1.64	0.225	10^{-4}

conducted using this material: 1. tensile tests at 850 °C and 2. static annealing tests at 850 °C. Specimens for tensile tests were produced with a gage width of 6.4 mm, a gage length of 25.4 mm, and a grip-gage transition radius of 1.6 mm. One hole 6.4 mm in diameter was centered in each specimen grip end to accommodate a pin for specimen loading. The original sheet thickness was retained, and the specimen tensile direction (TD) was always taken along the sheet rolling direction (RD). Tensile tests were conducted using a computer-controlled, servo-hydraulic test frame fitted with a three-zone resistance furnace and a fused quartz retort providing atmosphere control. Temperature control was calibrated to provide a specimen temperature of 850 °C within ±5 °C. Tensile specimens were tested in pin-loaded grips contained within the atmosphere-controlled retort at a constant true-strain rate of $\dot{\epsilon} = 10^{-4}$ s^{-1}, calculated assuming uniform gage region deformation. Strain was calculated from hydraulic piston displacement, and stress was calculated from force measured by a load cell. Tensile data were corrected for instrument compliance by enforcing the known elastic modulus of pure Fe at 850 °C, as reported by Köster.[47] Each specimen was elongated to a predetermined strain less than that at which significant necking or rupture was observed. The true strains achieved, calculated from gage length measurements taken before and after elongation, and other test conditions are summarized in Table II. Each specimen was heated to 850 °C within 30 minutes and subsequently soaked at this temperature for one hour to ensure complete recrystallization and a stable temperature prior to tensile straining. Experimental observations confirmed that this process produced fully recrystallized microstructures. Because of its very low carbon content in solution, the Ti-IF steel remains fully within the BCC ferrite phase field at 850 °C.[18] A constant load of 4.4 N was maintained on the specimen during heating and soaking, which produced a stress sufficiently small (≈ 1 MPa) to avoid significant creep deformation. Specimens were tested in a reducing atmosphere of N_2 with 4% H_2 to suppress oxidation. After straining at a constant true-strain rate to the target test strain, the computerized controller was changed from displacement to load control, and the specimen load was held constant while the specimen was rapidly quenched by impinging jets of pressurized air, a special feature of the custom instrumentation employed.[48] The average cooling rate from 850 °C to 200 °C was 80 °C/min. Quenching of the specimen while under load is critically important to preserving the microstructural features present during high-temperature deformation, particularly subgrain structures.

Static annealing experiments at 850 °C used the same instrumentation as the tensile tests, but without applying any strain, to induce recrystallization and SGG. Rectangular specimens 31 mm by 14 mm were excised from the Ti-IF sheet for static annealing tests. Each of four specimens was heated to 850 °C over 30 minutes, held at this temperature for a fixed time of at least one hour, and quenched to room temperature by air jets. Table II presents the conditions for these four tests.

Specimens were prepared for metallographic examination using typical grinding and polishing procedures, which included grinding on progressively finer SiC papers, polishing with progressively finer diamond suspensions, and final polishing with colloidal silica. Final polishing with a 0.05 μm colloidal silica suspension was performed for extended times, typically one hour. Microstructures were characterized by scanning electron microscope (SEM) using the backscatter electron (BSE) contrast and electron backscatter diffraction (EBSD) techniques. Crystallographic texture and the grain sizes of deformed and statically annealed specimens were evaluated from EBSD data. EBSD measurements on the deformed specimens employed a JEOL IT300HR SEM equipped with an EDAX Velocity EBSD detector. EBSD measurements on the statically annealed specimens employed a ThermoFisher Scientific Scios 2 focused ion beam SEM equipped with a Lumis EBSD detector. All SEM data were collected while operating with an accelerating voltage of 20 kV and a working distance between 10 and 20 mm. Specimens were tilted to 70 deg for EBSD measurements. EBSD data for normal analyses were collected with a step size of 0.75 μm using 4 × 4 camera binning and processed using the MTEX[49] toolbox for

MATLAB.[50] Grains were segmented using a minimum boundary misorientation angle of five degrees and a minimum grain area of 10 pixels (5.6 μm^2). These values were determined to produce the most reasonable segmentation of grains through testing a range of possible values. Unindexed points were filled based on neighboring grains, and noise reduction was applied using a half-quadratic minimization filter with $\alpha = 0.3$; see references 49 and 51 for details on this method. This choice of method and value of α, among all those available in MTEX, was determined to produce the most reasonable noise reduction without obscuring subgrain structures. Average grain area, A, was calculated for each specimen using the rectangular planimetric (Saltykov) method[52,53] applied to three EBSD data windows, each measuring 510 by 640 μm. Lineal intercept grain size, ℓ, was calculated from EBSD grain area measurements using the relationship recommended in ASTM E112-13[53]: $\ell = (\pi \bar{A}/4)^{1/2}$. Data for high-resolution EBSD (HR-EBSD) analysis, in which electron backscatter diffraction patterns (EBSPs) are saved for post-processing using image cross-correlation, were collected for deformed specimens on the JEOL IT300HR system using a step size of 0.5 μm and 1×1 camera binning (446×446 pixels). HR-EBSD provides a relative orientation resolution one to two orders of magnitude better than standard EBSD indexing methods that use the Hough transform.[54] This level of resolution is necessary to consistently resolve low-angle subgrain boundaries, as illustrated in Figure 3 using grain reference orientation deviation (GROD) maps.

The OpenXY[55] software package was used for cross-correlation-based HR-EBSD data processing. Regions of similar orientation were segmented by first identifying boundaries with a minimum misorientation angle of three degrees before processing data in OpenXY. Cross-correlation calculations were conducted independently within each segmented region. Experimental EBSPs, as opposed to dynamically simulated EBSPs, were used as reference patterns for the cross-correlation calculations. Band pass filters (OpenXY image filter values: 12, 55, 1, 1) were applied to the EBSPs to reduce image noise. The cross-correlation routine used 70 regions of interest per EBSP, each comprising 40% of the EBSP image area, equally spaced in an annular arrangement. No additional image filtering was applied. Outputs from the OpenXY cross-correlation calculations were saved for subsequent processing through the MTEX toolbox software. Software tools alone were found insufficient to accurately and reliably segment subgrains in the HR-EBSD data sets. Because of this, a combination of software and manual subgrain identification was used to measure subgrain sizes. First, the MTEX software was used to segment regions with boundary misorientations of two degrees or greater, and it did this reliably. No noise reduction was applied to HR-EBSD data processed using MTEX. Next, GROD maps were produced and used to manually identify subgrains that software could not segment. GROD maps provided the clearest visual distinction of subgrains among the many microstructure visualization methods examined. The number of subgrains identified completely within each HR-EBSD data set was counted for each test condition, and their corresponding total area coverage was measured. At least 80 subgrains were identified and counted for each test condition. From these measurements, average subgrain area was calculated for each test condition. Average lineal intercept subgrain size, λ, was calculated using the same relationship from ASTM E112-13[53] previously used to convert average grain area to average lineal intercept length. A disadvantage of this approach is the lack of a clear method to determine the uncertainty in subgrain size measurements without acquiring an impractically large number of HR-EBSD data sets. The misorientations of individual subgrain boundaries were measured in software after manually identifying all visible subgrains and specifying boundaries between adjacent subgrains. These measurements produced a distribution of individual subgrain misorientation angles for each test condition, from which an average subgrain misorientation angle was calculated.

The dihedral angle created by a subgrain boundary intersection with a high-angle grain boundary, illustrated in Figure 2(d), and the misorientation across the intersecting subgrain boundary are quantities of particular interest for the present investigation. To measure these, several such intersections were identified from

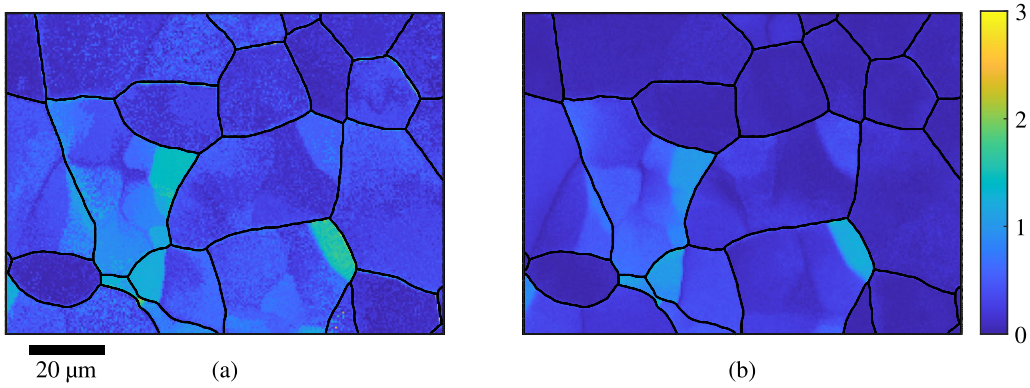

Fig. 3—Grain reference orientation deviation (GROD) maps revealing subgrains are calculated from (*a*) standard EBSD data based on Hough transform indexing and (*b*) HR-EBSD data based on EBSP cross-correlation. HR-EBSD provides higher relative orientation resolution and reduces noise compared to standard EBSD. The microstructure shown is in Ti-IF steel after straining to $\epsilon_f = 0.086$ at $\dot{\epsilon} = 10^{-4}$ s^{-1} and 850 °C (Color images are available online).

specimens tested to three different true strains: 0.086, 0.124, and 0.225. One example is shown in Figure 4(a). Both HR-EBSD data and BSE images were acquired at these locations. HR-EBSD data were used to measure subgrain boundary misorientations, and high-magnification BSE images were used to measure dihedral angles. The method for making these measurements is illustrated in Figure 4. The average misorientation across each boundary was calculated from five orientation measurements made in each of the three unique grain or subgrain regions illustrated in Figure 4(b). The dihedral angle, ϕ, induced in the high-angle grain boundary was measured from a high-resolution BSE image, as illustrated in Figure 4(c). At least 16 such measurements were made for each of the three test conditions examined.

IV. RESULTS

Microstructural characterization confirmed that Ti-IF steel specimens fully recrystallized during the one-hour soak at 850 °C prior to tensile straining. Figure 5 presents a typical plot of true stress *versus* true strain for a tension test conducted at $\dot{\epsilon} = 10^{-4}$ s^{-1} and 850 °C. Noise in the load data was reduced by applying a third-order Butterworth low-pass filter with a 2 min^{-1} cutoff. Flow stress is steady for true strains greater than $\epsilon \approx 0.03$. The steady-state flow stress averaged over all specimens tested is 11.1 ± 1.9 MPa. Flow stress remains steady up to the highest strain investigated, $\epsilon = 0.225$, indicating homogeneous deformation by steady-state creep in this testing regime.[26] No necking or otherwise inhomogeneous deformation was observed in specimen gage regions. A small amount of deformation was measured near the pin holes used for loading the specimens during tensile testing. Accounting for this effect, the average true-strain rate during deformation was calculated to be within the range of 7.5×10^{-5} to 10^{-4} s^{-1}.

Figure 6 presents microstructures in specimen plane sections that include the tensile direction (TD = RD) and the long-transverse direction (LTD), viewed along the short-transverse direction (STD). Inverse pole figure (IPF) maps display the differences between microstructures produced by static annealing, in the left column, and those produced by the dynamic test conditions during tensile deformation, in the right column. These IPF maps are colored with respect to

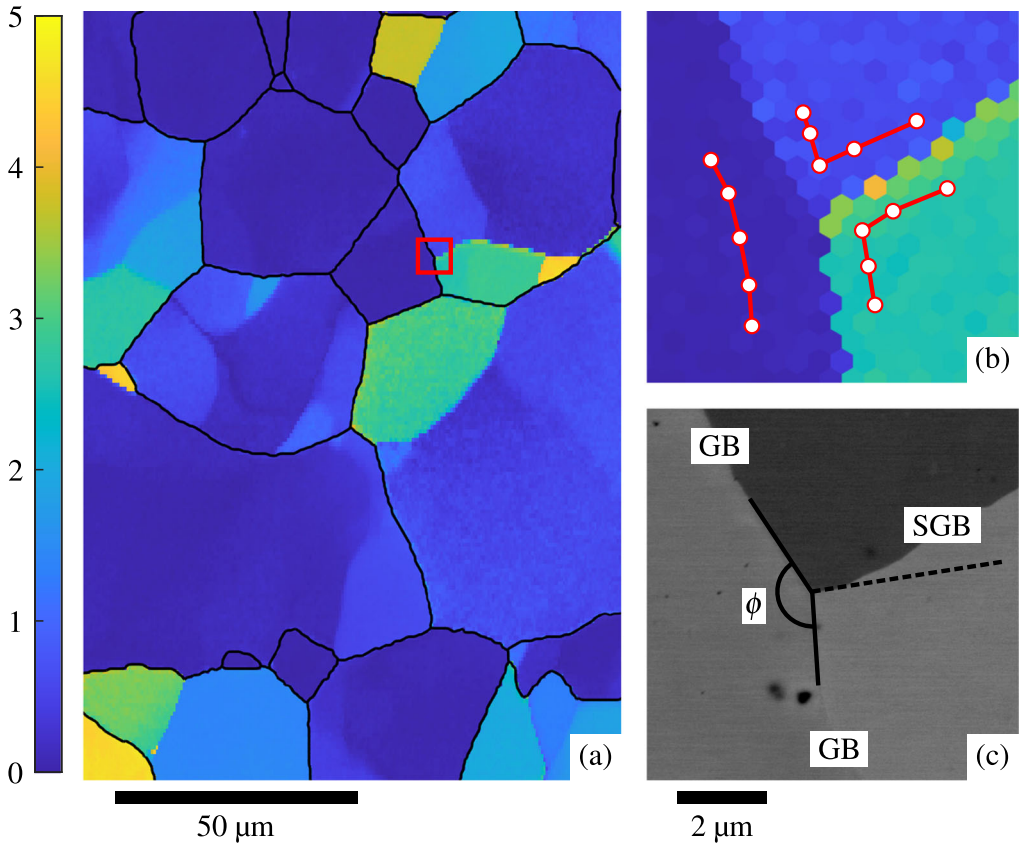

Fig. 4—(*a*) Subgrain boundary intersections with grain boundaries are visible in this GROD map from HR-EBSD data for Ti-IF steel strained to $\epsilon_f = 0.225$ at $\dot{\epsilon} = 10^{-4}$ s^{-1} and 850 °C. A red box marks the region of interest shown in (*b*) and (*c*) at higher magnification. (b) Locations of orientation measurements used for calculating boundary misorientations are marked. (c) The dihedral angle, ϕ, is measured from a BSE image. Facets of the high-angle boundary between which ϕ is defined are marked with solid lines, and a dashed line marks the orientation of the subgrain boundary facet at its intersection with the high-angle boundary. The scales of images (b) and (c) are identical (Color images are available online).

the STD. Grain boundaries defined by misorientation angles greater than five degrees are traced by solid lines. Only modest grain growth is apparent between static annealing for one and eight hours. The deformed microstructures exhibit much larger grains than either of the statically annealed microstructures. Significant grain growth is apparent between the specimens deformed to true strains of 0.086 and 0.225. Subgrains are numerous in the deformed microstructures, but regions similarly delimited by low-angle boundaries formed during recrystallization, which may also be called subgrains, are nearly absent from the recrystallized and statically annealed microstructures. For example, the undeformed microstructure at the bottom of Figure 6 ($t = 8$ hrs) contains an average of 0.09 subgrains per grain, and the deformed microstructure beside it ($\epsilon_f = 0.225$) contains an average of 0.6 subgrains per grain. Subgrain boundaries are sometimes visible in IPF maps as sharp color changes within a grain. Subgrains are most prominent in the specimen with the largest plastic strain, which suggests that crystallographic misorientation across subgrain boundaries increases with increasing strain.

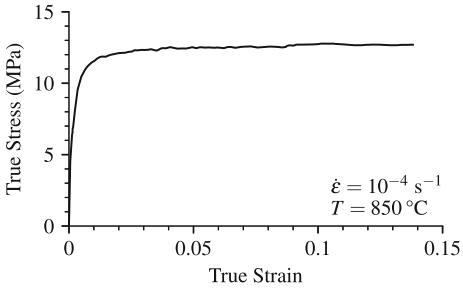

Fig. 5—Typical tensile test data are plotted as true stress *versus* true strain for Ti-IF steel deformed in uniaxial tension at $\dot{\epsilon} = 10^{-4}$ s^{-1} and 850 °C.

Recrystallization produced a strong $\langle 111 \rangle \parallel$ STD texture component belonging to the γ-fiber, which is evident in both the statically annealed and deformed microstructures of Figure 6. The inverse pole figures presented in Figure 7 more clearly demonstrate this γ-fiber component and reveal a strong $\langle 110 \rangle \parallel$ RD/TD texture component belonging to the α-fiber. The strength of this α-fiber component increases with plastic strain, while the

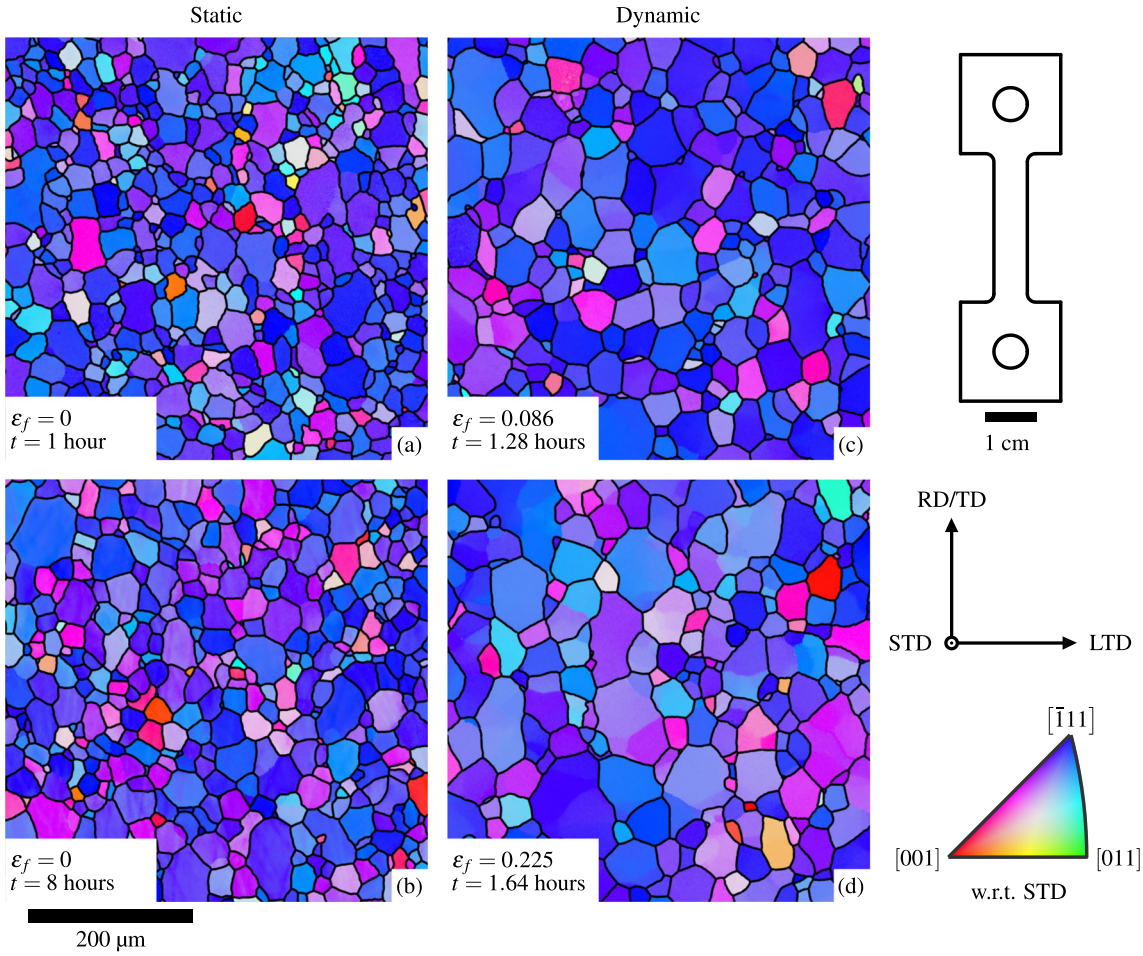

Fig. 6—IPF maps are shown for Ti-IF steel microstructures produced at 850 °C by static annealing for (*a*) 1 h and (*b*) 8 h and by tensile straining at $\dot{\epsilon} = 10^{-4}$ s^{-1} to (*c*) $\epsilon_f = 0.086$ and (*d*) $\epsilon_f = 0.225$. All IPF maps are at the same scale. A scale representation of the tensile coupon geometry is shown at the right with specimen reference directions. These demonstrate the orientation of IPF maps with respect to the specimen reference directions (Color images are available online).

strength of the γ-fiber component is only slightly diminished. These results are consistent with the detailed analysis by Rupp *et al.* for the effects of recrystallization, plastic straining, and DGG on the crystallographic texture in this material.[18] A map of the Taylor factor under uniaxial tension applied along the RD is presented in Figure 7 for comparison. The Taylor factor was calculated for uniaxial tension assuming mixed slip on the $\{110\}\langle\bar{1}11\rangle$, $\{112\}\langle11\bar{1}\rangle$, and $\{123\}\langle11\bar{1}\rangle$ slip systems.[56] Examination of the Taylor factor map indicates that α-fiber texture components are associated with high Taylor factors. Thus, texture components associated with high Taylor factors were strengthened by uniaxial tensile deformation at 850 °C.

Lineal intercept grain sizes, converted from EBSD grain area measurements, are presented in Figure 8(a) as a function of the logarithm of time at 850 °C. Times at this temperature reported for the dynamic specimens include the one-hour soaking time before plastic straining. Error bars indicate the minimum and maximum values from each set of three measurement fields. Grain size increased steadily with time at temperature in statically annealed specimens. The average grain size was 19.9 ± 0.2 μm after one hour of static annealing at 850 °C and 22.5 ± 1.2 μm after eight hours. Dynamic conditions produced significantly larger grain sizes than did static annealing. Figure 8(b) presents average grain size from dynamic tests as a function of true strain. Error bars have the same meaning as in Figure 8(a). At $\epsilon = 0.076$, the lineal intercept grain size was 27.7 ± 0.5 μm. At $\epsilon = 0.225$, the grain size increased to 33.9 ± 0.6 μm. From the smallest nonzero strain to the largest strain investigated, grain size increases approximately linearly with true strain. The rate of this

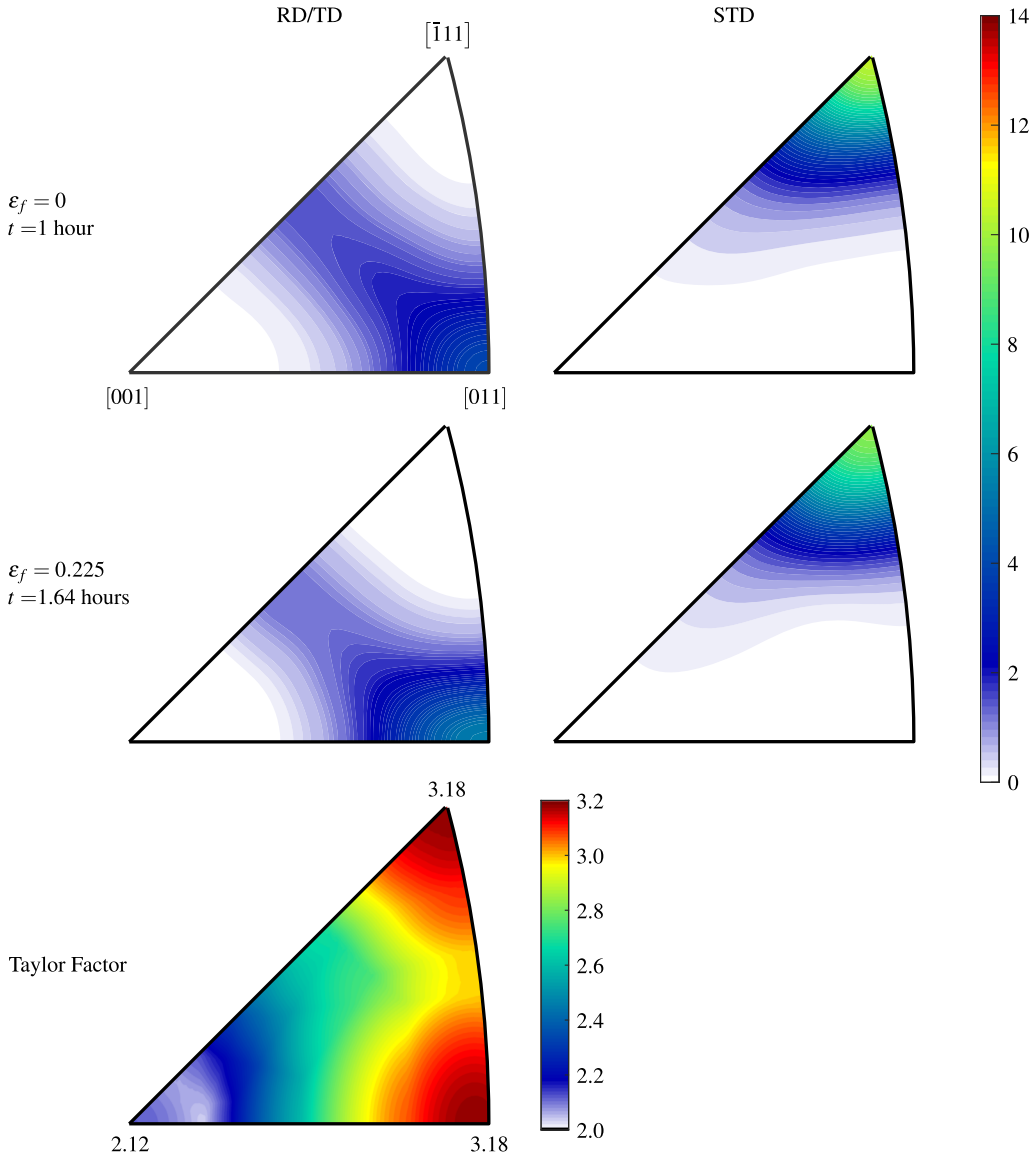

Fig. 7—Inverse pole figures (IPFs) demonstrate the change in texture from the statically annealed material to the deformed material. A Taylor factor map, calculated for uniaxial tension assuming mixed slip on the $\{110\}\langle\bar{1}11\rangle$, $\{112\}\langle11\bar{1}\rangle$, and $\{123\}\langle11\bar{1}\rangle$ slip systems, is shown for reference (Color images are available online).

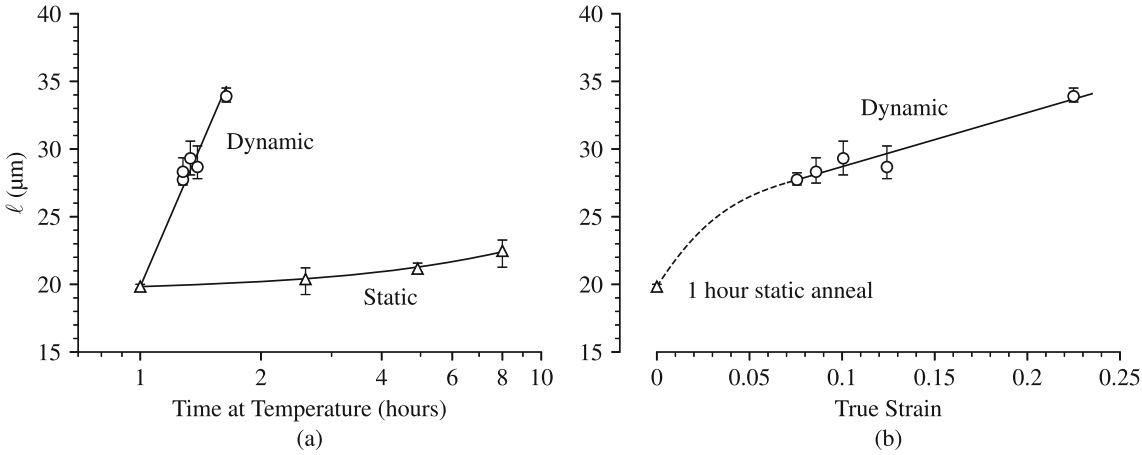

Fig. 8—Lineal intercept grain size, ℓ, is plotted as a function of (*a*) time at temperature and (*b*) true strain. The grain size produced by static annealing for one hour is representative of the grain size at zero strain.

increase, as measured from the slope of the solid regression line shown in Figure 8(b), is 39.9 μm per unit strain. The data of Figure 8(b) suggest that grain growth is initially faster than this but quickly slows to the observed steady growth rate after initial straining, as suggested by the dashed curve.

Figure 9 presents measurements of individual grain areas as histograms on a logarithmic scale. These histograms present the number fraction of grains belonging to each grain area interval, with the sum of the bar heights normalized to unity. This number fraction representation is used to clearly present populations of small grains that would be diminished in an area fraction representation. Only grains completely captured in EBSD data were included in these calculations, *i.e.*, grains intersected by the border of a data set were excluded. The number of grains sampled, N, is shown in the top left corner of each histogram. Over 1600 grains were sampled from each of the statically annealed specimens. At least 500 grains were sampled from each dynamic specimen; the smaller sample numbers for dynamic specimens are results of their larger grain sizes. Grain area distributions are interpreted here as approximately log-normal with a single dominant mode. All the grain area distributions exhibit long left tails, but the long left tails are most pronounced for dynamic conditions. These results are consistent with those of Rupp *et al.*,[18] who interpreted the grain size distributions following DGG as bimodal with the smaller mode at small grain sizes. The alternative approach of measuring skewness is used here to distinguish between the grain area distributions produced by SGG and DGG. Skewness, the third standard moment about the mean, quantifies deviation from a normal distribution and is useful for quantifying the relative sizes of the left tails observed in Figure 9. The sample skewness is defined as,[57]

$$S = \frac{\sqrt{N(N-1)}}{N-2}\frac{1}{N}\sum_{i=1}^{N}\left(\frac{x_i - \bar{x}}{\sigma_{sd}}\right)^3 \qquad [10]$$

where $\bar{x}$ and σ_{sd} are the mean and population (biased) standard deviation. In this case, $x_i = \log_{10}(A_i)$ where A_i is the grain area of the ith grain. For negative skewness, larger absolute values indicate longer left tails. Skewness values, calculated from the logarithms of grain area, are reported for each distribution in Figure 9. The magnitude of the average skewness produced by DGG, $\bar{S}_{dgg} = -0.71 \pm 0.09$, is significantly greater than that produced by SGG, $\bar{S}_{sgg} = -0.44 \pm 0.10$, where the uncertainty in these averages is represented by the sample standard deviation. Skewness does not appear to change significantly with annealing time in the statically annealed specimens. Neither does skewness appear to change significantly, or at least consistently, with strain in the dynamic case.

Figure 10(a) presents average lineal intercept grain size, ℓ, and subgrain size, λ, as functions of true strain. Across the range of strains investigated, subgrain size remains constant with an average value of 19.4 ± 0.9 μm; uncertainty in this average is represented by the standard deviation. A constant subgrain size is expected for steady-state, five-power creep in a BCC or otherwise high-stacking-fault-energy metal deformed at a constant true-strain rate and responding with a constant flow stress.[25,26,28,30,31,58–62] As previously described, the method used to measure subgrain size does not produce a value for uncertainty, which is the reason that error bars are absent for subgrain sizes reported in Figure 10(a). Figure 10(b) presents average subgrain boundary misorientation angle as a function of true strain. Error bars are not provided in Figure 10(b) because uncertainty in the measurements of $\bar{\theta}_{sgb}$ are best evaluated using the histograms presented in Figure 11. Subgrain boundary misorientation increases with increasing true strain, but the rate of increase diminishes as strain increases. A straight-line extrapolation of subgrain boundary misorientation angle to zero strain suggests that nonzero subgrain boundary misorientation angles form only after a plastic true strain of approximately 0.06. Subgrains are expected to achieve relatively stable sizes upon the transition from primary to

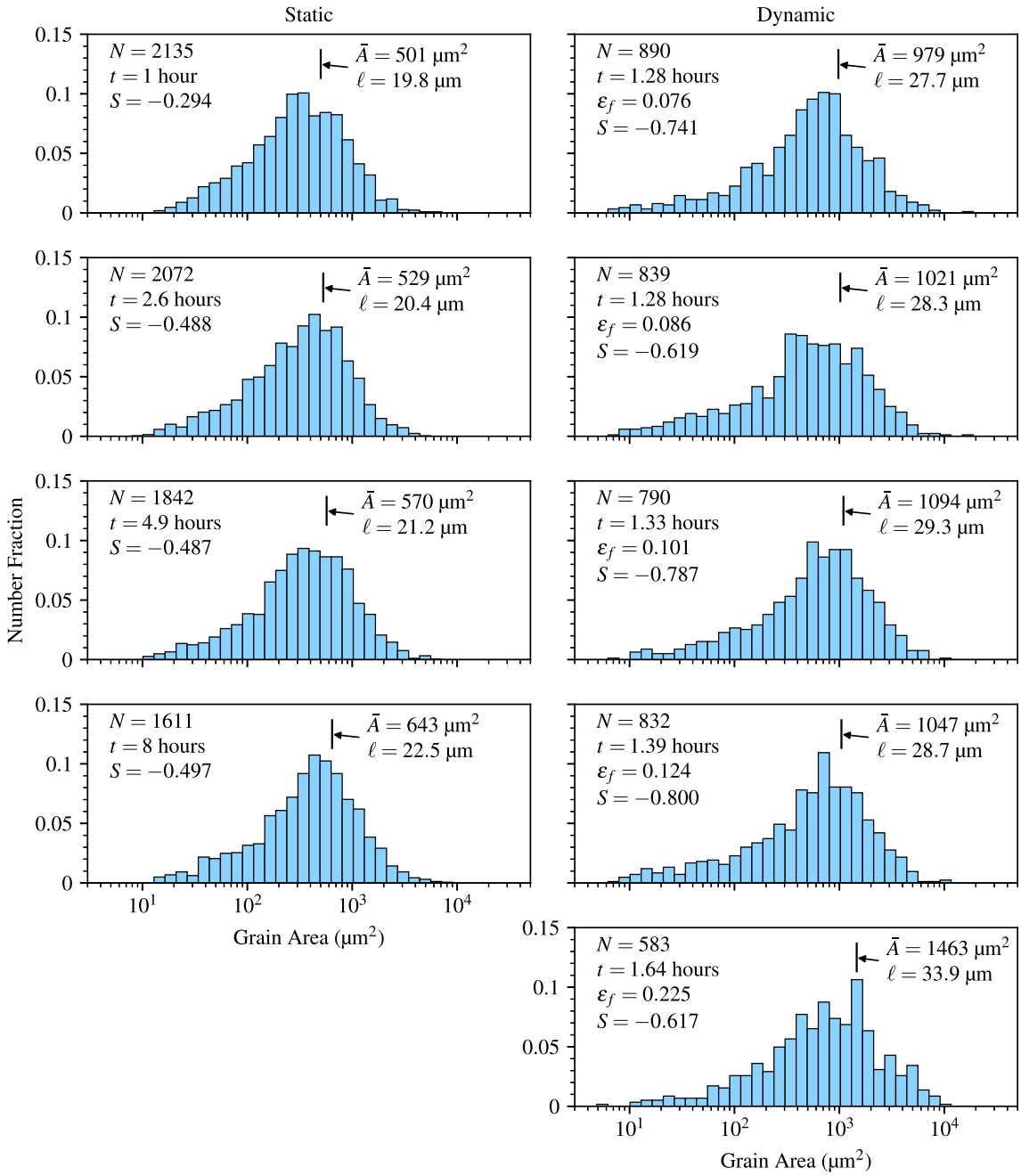

Fig. 9—Distributions of grain areas, calculated from EBSD data, are shown for Ti-IF steel microstructures produced under static (left column) and dynamic (right column) test conditions. The number of grains sampled, N, and the sample skewness, S, are reported. Time at temperature, t, and final true strain, ϵ_f, are reported where applicable.

steady-state deformation, which occurs at a true strain of approximately 0.03 according to the data presented in Figure 5. This suggests that the increase in subgrain boundary misorientation at small strains just beyond the transition into steady-state deformation is nonlinear with strain. These data also suggest that even very small subgrain boundary misorientations are associated with steady-state flow under plastic deformation at a prescribed true-strain rate and constant temperature. This evolution in subgrain boundary misorientation with strain is similar to that measured by Kassner and McMahon in unalloyed aluminum.[31]

Figure 11 presents histograms of the logarithm of subgrain boundary misorientation angle, θ_{sgb}, for each of four plastic strains. These histograms are scaled so the bar heights sum to unity. The number of subgrain boundaries measured, N, and the plastic strain applied are reported in each histogram. The average subgrain boundary misorientation angle, $\bar{\theta}_{sgb}$, is indicated for each test condition. All distributions are approximately log-normal, which is evident from the log-normal fits

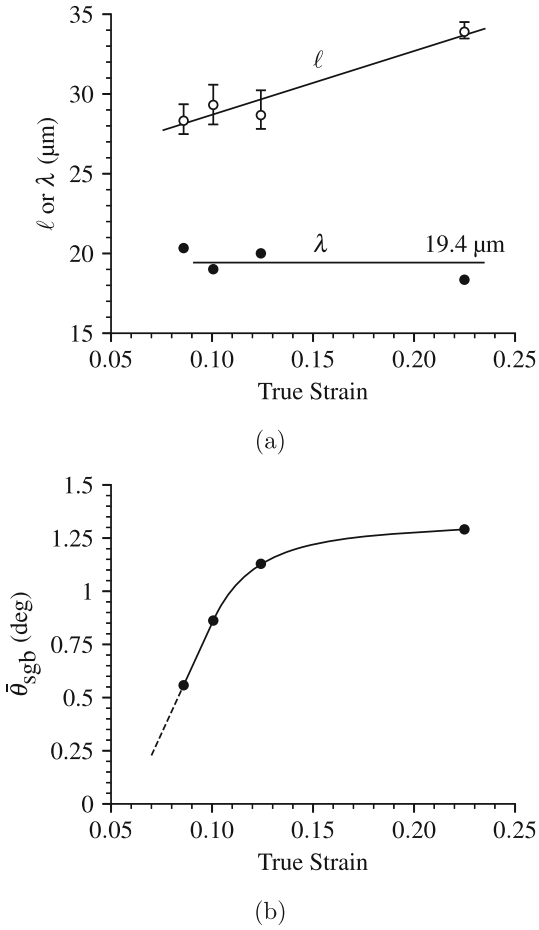

Fig. 10—(*a*) Average lineal intercept grain size, ℓ, and subgrain size, λ, are plotted against true strain. (*b*) Average subgrain boundary misorientation angle, $\bar{\theta}_{sgb}$, is plotted against true strain.

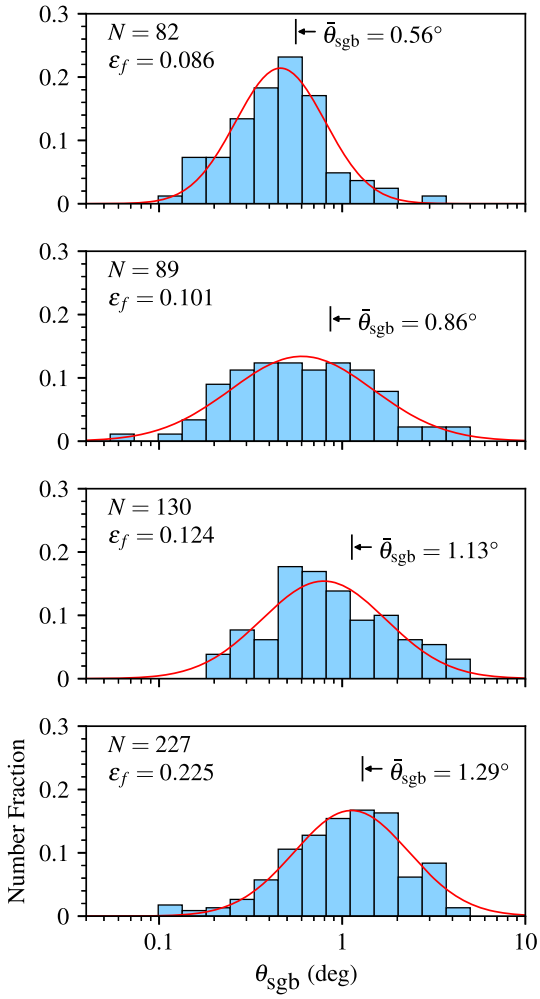

Fig. 11—Measured subgrain boundary misorientation angles are presented as histograms with the average misorientation angle marked for each of four test conditions. The number of measurements made, *N*, and the true strain imposed on the specimen, ϵ_f, are presented for each data set. Red curves are log-normal fits to the data (Color figure online).

plotted over the histograms. The subgrain boundary misorientation distributions shift toward larger angles as strain increases. The right tail of the histogram at the highest strain investigated, $\epsilon = 0.225$, is slightly truncated by the 5 deg threshold for distinguishing subgrain boundaries from grain boundaries, but the effect from this is considered negligibly small for the present analysis.

V. DISCUSSION

A. *Plastic Flow and Subgrain Evolution*

High-resolution information from EBSD data for relative crystallographic misorientations provides a new opportunity to assess the role of subgrains in plastic flow and DGG phenomena at elevated temperatures. The plastic flow behaviors observed in Ti-IF steel are consistent with prior work[18] that demonstrated flow dominated by five-power creep at a true-strain rate of 10^{-4} s^{-1} and temperature of 850 °C. The representative stress–strain data in Figure 5 display an expected initial flow transient, the equivalent of standard primary creep, that quickly subsides into steady-state flow, which persists from a true strain of approximately 0.03 until test completion. Subgrains are expected to evolve during the initial flow transient and reach a stable size that is inversely proportional to the flow stress during steady-state deformation.[25–27] Microstructures at the smallest strain examined, $\epsilon = 0.076$, evidence distinct subgrains with a mature size that remains constant at $\lambda = 19.4$ μm up to the largest strain evaluated, $\epsilon = 0.225$. This constant subgrain size is consistent with a constant flow stress proportional to the inverse of subgrain size ($\sigma \propto 1/\lambda$) during steady-state, five-power creep.[26,27] Although DGG produces a nearly linear increase in grain size with strain, shown in Figures 8(b) and 10(a), it does not affect the flow stress. This is expected because flow stress during steady-state, five-power creep is essentially invariant with grain size, except for very small ($\ell \lesssim \lambda$) and very large grain sizes.[26,27,63] Although subgrain size does not change with strain during steady-state flow, subgrain boundary misorientation clearly increases with increasing strain. Figures 10(b) and 11 demonstrate the increase of $\bar{\theta}_{sgb}$

with strain at a rate diminishing beyond 0.1 true strain. Clearly, subgrain size controls flow stress effectively at even small subgrain boundary misorientations ($\bar{\theta}_{sgb} < 0.5°$).

The HR-EBSD technique applied here offers several advantages over previously established techniques for characterizing subgrains produced during high-temperature deformation. Historically, subgrains were characterized using either optical microscopy (OM), transmission electron microscopy (TEM), or X-ray diffraction.[26,27,29,31] OM presents difficulties with distinguishing subgrain boundaries from high-angle grain boundaries. The secondary electron and BSE imaging techniques of SEM present a similar limitation. TEM can provide clear distinctions between low- and high-angle boundaries and can be used to measure boundary misorientations, but it is laborious for acquiring statistically significant numbers of measurements. X-ray diffraction techniques can measure features from populations of subgrains,[29] but only the most powerful of recently developed techniques allow measurements of individual subgrains. By coupling EBSD measurements with the increased angular resolution of HR-EBSD analysis, many of these previous limitations are overcome. Low- and high-angle boundaries are easily and quantitatively distinguished, a large number of measurements can be made, and boundary misorientation measurements are directly tied to specific subgrains. While the cross-correlation HR-EBSD technique is very effective in the present study, new software techniques for EBSP indexing using spherical harmonics[64,65] may provide sufficient accuracy for similar analyses in future studies with a lower computational burden.

B. *Dynamic Grain Growth*

SGG in the Ti-IF steel proceeded very slowly with annealing time. The difference in average lineal intercept grain size after one and eight hours of static annealing at 850 °C was 2.7 μm, an increase of only 13%. This result is not surprising. Ti is alloyed in this ultra-low-carbon steel to scavenge interstitial elements and produce an interstitial-free matrix. These scavenged interstitials combine with Ti to form precipitates, principally TiC, which pin grain boundaries.[66] This reduces boundary mobility. Because SGG was observed, even the driving pressures for boundary migration present in the static case are sufficient to overcome some fraction of pinning locations, *i.e.*, $m > 0$ in Eq. [1].

Significant DGG was observed in the specimens plastically deformed at 850 °C. Only dynamic normal grain growth occurred; no abnormal grains were observed in the deformed specimens. All deformed specimens, each of which was at temperature for less than 100 min, had grain sizes larger than the specimen statically annealed for eight hours. The specimen deformed to $\epsilon_f = 0.225$ was at temperature for 1.64 hours and produced an average lineal intercept grain size of 33.9 μm, which is 71% larger than the grain size produced after one hour of static annealing. The faster rate of grain growth associated with DGG suggests a greater driving pressure on boundaries, such as proposed in Eq. [6], and/or an increased boundary mobility, such as through the unpinning mechanism proposed by Bate and Hyde.[7,8,23] Data from the present study provide an opportunity to test the role of subgrains in increasing the driving pressure during DGG. The data, however, do not provide a means of directly evaluating mobility differences between SGG and DGG.

Both static and dynamic normal grain growth produced generally equiaxed microstructures with grain aspect ratios in the range of 1.55 to 1.6 for all test conditions. The grain sizes observed after SGG and DGG are reasonably characterized by log-normal grain area distributions with elongated left tails, as shown in Figure 9. The long left tails of these distributions likely represent a population of small grains not favored for growth. DGG produced wider grain area distributions with more negative skewness than did SGG. This suggests that a significant population of small grains are not favored for growth and are left unconsumed by growing grains under dynamic conditions. Examples of such small grains are evident in the microstructures of the deformed (dynamic) specimens shown in Figure 6.

DGG produced under uniaxial tension along the RD produces the following crystallographic texture changes: 1. strengthening of α-fiber components and 2. slight weakening of γ-fiber components. An analysis of this texture evolution by Rupp *et al.*[18] demonstrated that crystal rotation under plastic deformation is associated with strengthening of α-fiber components and weakening of the γ-fiber components not intersecting the α-fiber. The same analysis demonstrated that DGG makes a unique texture contribution by strengthening the γ-fiber, particularly the $\{111\}\langle 1\bar{1}0\rangle$ and $\{111\}\langle 11\bar{2}\rangle$ components. Onuki *et al.*[24] proposed a "preferential dynamic grain growth mechanism" by which grains preferred for DGG are those oriented for stability and low Taylor factors under the imposed deformation. The present observations are in generally good agreement with the first assertion of this hypothesis. Changes in texture are consistent with preferential growth of grains oriented for stability under deformation. However, the second assertion of the hypothesis of Onuki *et al.* is inconsistent with the present results. The unique texture components strengthened by DGG are oriented for relatively high Taylor factors. The data suggest that crystal rotation and stability against deformation are more significant than the Taylor factor in controlling texture evolution during DGG.

C. *Driving Pressures for Grain-Boundary Migration*

A theoretical model was described by which subgrain boundary intersections with high-angle grain boundaries can produce a driving pressure for grain-boundary migration, thus, driving DGG. In order to assess the feasibility of this model, quantitative predictions of driving pressure are compared against driving pressures estimated from classical models, namely grain boundary curvature and dislocation density reduction. First

estimated is the driving pressure from classical grain boundary curvature theory, $P_{gb} = 2\gamma_{gb}/R$, where R is the radius of curvature.[20] Estimating this driving pressure requires information for the grain boundary energy. Energies for high-angle grain boundaries in BCC Fe determined from experiments and computational simulations are summarized in Table III.[45,67–74] When an average value was not reported by the authors, the values presented are averages across large misorientation angles, *e.g.*, $30 \leq \theta \leq 60$ for Jaatinen *et al.*,[72] excluding any exceptionally low energy boundaries. The standard deviations of these calculations are reported where feasible. Although grain boundary energy can vary with boundary misorientation, the experimental work of Dunn *et al.* demonstrates that the ratio of grain boundary energy to surface energy in BCC Fe plateaus above a boundary misorientation angle of approximately 20 deg.[75,76] The simulations of ⟨100⟩ tilt boundaries by Jaatinen *et al.* predict a similar effect.[72] The embedded atom method used by Ratanaphan *et al.* predicts that grain boundary energy is relatively constant across many different boundary types of large misorientation angle, with the specific exception of boundaries sharing (110) planes, which are of particularly low energy.[73] The computationally predicted values at the bottom of Table III demonstrate a wider variation than the experimental values reported at the top of this table. The experimentally measured grain boundary energies for BCC Fe, which range from 0.46 to 0.99 J/m^2, are used to predict the driving pressure from grain boundary curvature. Assuming that the radius of boundary curvature is half the recrystallized grain size of 20 μm, the driving pressure for grain-boundary migration from boundary curvature is estimated to be in the range of 0.09 to 0.20 MPa. Because faceting of grain boundaries will generally produce radii of curvature larger than half the grain size, as is clear from Figure 1, this estimate is best considered an upper bound. Because the recent investigation of Bhattacharya *et al.*[21] found no correlation between grain boundary curvature and migration velocity in polycrystalline Ni, it is possible that the actual driving force from grain boundary curvature is so small as to be negligible. Thus, an upper bound is estimated for the driving pressure from grain boundary curvature, but reality may be closer to a lower bound of almost zero. This range of possible driving pressures is reflected in Table IV. It is important to note that any pressure from grain boundary curvature will occur in *both* the static and dynamic cases with similar effect and, thus, cannot be responsible for the difference in SGG and DGG rates. This difference in rates must result from effects that are different between the static and dynamic cases, such as the boundary migration pressures from dislocation density reduction and subgrain boundary intersections, which are considered next.

An estimate of driving pressure for boundary migration based on dislocation density reduction is next considered. This requires values for temperature-dependent shear modulus and dislocation density. The driving pressure due to dislocation density reduction is estimated by applying Eq. [2]. Using the values and methodology recommended by Frost and Ashby,[77] the shear modulus of BCC Fe is calculated to be 27.9 GPa at 850 °C, and the Burgers vector length is assumed to be 2.48×10^{-10} m. Dislocation density can be estimated from the data of Barrett *et al.*[25] and Karashima *et al.*[28] Barrett *et al.* reported dislocation densities within subgrains to range from 7×10^{11} to 1.7×10^{12} m^{-2} in creep of Fe-3Si (wt pct). Karashima *et al.* reported dislocation densities within subgrains to range from 4×10^{11} to 10^{12} m^{-2} in the creep of single-crystal α-Fe. Their data indicate a dislocation density of approximately 5×10^{11} m^{-2} at the average steady-state flow stress of 11 MPa observed in the present study. Note that the dislocation density within subgrains during steady-state, five-power creep is a function of stress but not temperature.[27,28] Dislocation densities within subgrains are observed to vary with stress approximately in accordance with the Taylor relation ($\sigma \propto \sqrt{\rho}$) during five-power creep.[26,27] Using these data, the driving pressure for grain-boundary migration from the reduction of dislocation density within subgrains is predicted to be 4×10^{-4} MPa, which is shown in Table IV.

A quantitative estimate of the driving pressure on grain boundaries due to subgrain boundaries is now considered. The predictions of Jaatinen *et al.* are used here because they present boundary energies in BCC Fe across a range of low-angle boundaries and recommend best-fit parameters for the Read-Shockley equation, Eq. [9], of $\gamma_0 = 1.1271$ J/m^2 and $A_{RS} = -0.41$.[72] This fit is quite good for boundary misorientations up to approximately 10 deg. It is important to note that the values predicted by Jaatinen *et al.* for grain boundary energy are lower than the experimental values and those of other numerical simulations. The subgrain boundary energies thus predicted for misorientation angles from 0.6 to 1.3 deg, the range of angles experimentally measured and reported in Figure 10(b), likely represent lower bounds on actual energies. The spacing of subgrain boundary intersections with grain boundaries, L in Figure 2(c), is assumed equal to 20 μm, approximately the mean lineal intercept subgrain size. Using these approximations, the driving pressure is predicted to range from 2×10^{-3} to 4×10^{-3} MPa, as reported in Table IV. This is one order of magnitude greater than the pressure estimated from the reduction of dislocation density within subgrains. Thus, boundary migration pressure from subgrain boundary intersections is the more likely mechanism to cause the faster grain growth observed under dynamic conditions. It is noted that the pressure from subgrains is two orders of magnitude less than the upper bound estimated from classical grain boundary curvature but far greater than the lower bound suggested by the results of Bhattacharya *et al.*[21] The much slower rate of static grain growth suggests that the pressure from boundary curvature, which is present in both the static and dynamic cases, is likely toward the lower values of that range and less than the pressure from subgrains, if boundary mobility is similar for both cases.

The following process by which subgrain boundaries drive DGG can now be envisioned. As subgrains develop with strain under five-power creep, their

Table III. Experimentally and Computationally Determined Grain Boundary Energies for BCC Fe

γ_{gb} (J/m^2)		Experimental Conditions	Source
0.985		δ-Fe at 1480 °C	Roth[67]
0.795		δ-Fe at 1450 °C	Hondros[68]
0.470		δ-Fe at 1400–1535 °C	Price *et al.*[69]
0.468		δ-Fe at 1450 °C	Murr[70]
0.462		α-Fe-3Si (wt pct) at 1330 °C	Hondros and Stuart[71]
γ_{gb} (J/m^2)		**Computational Methods**	**Source**
1.58	±0.20	DFT tight binding model: various boundaries	Wang *et al.*[74]
1.30		estimated from elastic constants: tilt boundary	Shockley and Read[45]
1.11	±0.209	embedded atom (LAMMPS): various boundaries	Ratanapha *et al.*[73]
0.372	±0.005	phase field crystal model: ⟨100⟩ tilt boundaries	Jaatinen *et al.*[72]

Table IV. Predicted Driving Pressures for Grain-Boundary Migration in BCC Fe

Mechanism	P (MPa)
Grain Boundary Curvature	$0 \leq P_{gb} \leq 0.2$
Dislocation Density Reduction	$P_d \approx 4 \times 10^{-4}$
Subgrain Boundary Intersections	$2 \times 10^{-3} \leq P_{sgb} \leq 4 \times 10^{-3}$

boundary misorientation angles increase, which is demonstrated in Figure 10(b). Increasing misorientation angle increases the subgrain boundary energy according to the Read-Shockley equation, Eq. [9], which increases the driving pressure for boundary migration, as predicted by Eq. [6]. When an imbalance in driving pressure across a grain boundary occurs, as predicted by Eq. [7], one grain will grow at the expense of its neighbor. All subgrain boundaries within the consumed grain are eliminated. The growing grain may be expected to retain its preexisting subgrain boundaries during growth, but it is unlikely to gain new subgrain boundary area. Thus, the growing grain will have a lower subgrain boundary area per unit volume, and a larger effective subgrain size, after growth. To restore the approximately constant subgrain size across the microstructure, as demonstrated in Figure 10(a), new subgrain boundary area must be accumulated with strain in a grain following its growth. The new subgrains that develop will begin with very low boundary misorientation angles that increase with strain, as suggested by the trends in Figures 10(b) and 11. The following might be expected from this process. 1. After a grain grows, it will have an increased subgrain size and will develop subgrain boundaries with small boundary misorientations. This will bias the same grain for further growth at the expense of its neighbors that retain smaller subgrains with higher boundary misorientations. 2. The dynamic evolution of subgrains between growing and shrinking grains could slow the rate of increase in subgrain boundary average misorientation with strain. This may be a cause for the decreasing slope of $\bar{\theta}_{sgb}$ with strain in Figure 10(b). 3. Any differences in subgrain evolution between grains may bias some grains for growth at the expense of their neighboring grains.

It is worth noting that the process envisioned above may explain an important previous observation for dynamic abnormal grain growth, DAGG, in the refractory metals Mo and Ta.[11–17] DAGG is a dynamic grain growth process by which one or a few grains grow at the expense of all other grains in a microstructures. A minimum strain, termed the critical strain, is required to initiate DAGG.[11–17] This critical strain is a function of strain rate, temperature, and material composition/microstructure. The propensity of a dynamically growing grain to continue its growth under the influence of subgrain boundaries, predicted in item 1 of the preceding paragraph, may encourage abnormal grain growth. The critical strain for DAGG may be a result of the increasing driving pressure from subgrains with increasing strain, as described in the previous paragraph, reaching a minimum value to initiate the DAGG process.

A directly testable prediction of the proposed model for grain-boundary migration is the dihedral angle, ϕ, subtending grain boundary cusps formed at subgrain boundary intersections, as shown in Figures 2(c) and (d) and predicted by Eq. [8]. Calculating ϕ involves only relative boundary energy values. Simulation predictions for relative values may be more comfortably relied upon than absolute values of boundary energy. The grain boundary energy and Read-Shockley parameters of Jaatinen *et al.* were used to predict the dihedral angles at subgrain boundary intersections with high-angle grain boundaries as a function of θ_{sgb}. Predicted values of ϕ were calculated for values of θ_{sgb} ranging from 0.1 to 5 deg. Experimental values of ϕ and θ_{sgb} were measured from BSE images and HR-EBSD data, respectively.

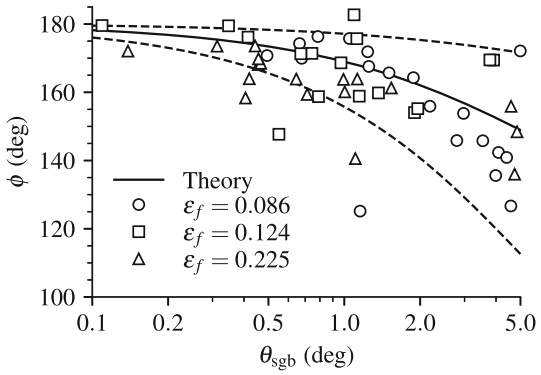

Fig. 12—Predictions from theory and measured dihedral angles are plotted against subgrain boundary misorientation angle. The dashed lines are predictions to bound 95% of measured dihedral angles assuming subgrain boundary intersections at grain boundaries are randomly oriented.

Figure 12 shows experimental and predicted values of ϕ plotted as a function of θ_{sgb}. The solid curve indicates predicted dihedral angles, and the symbols indicate experimental values from specimens deformed to three different strains. It is important to note that the dihedral angle was measured experimentally from a plane section, and this measured angle, ϕ, is not necessarily equal to the true dihedral angle, ϕ_T, in three-dimensional space. Butler and Reeds[78,79] considered the stereological problem of measuring dihedral angles projected onto a plane in a medium containing randomly oriented wedges of a fixed dihedral angle. The distribution of ϕ at a fixed value of ϕ_T is a complicated function of elliptic integrals that is derived in Reference 79. This distribution function was implemented numerically for the present study using the algorithms of Carlson and Notis[80,81] to evaluate the elliptic integrals. Upper and lower bounds predicted to contain 95% of ϕ values for a fixed ϕ_T were calculated by inverting the distribution function for ϕ numerically. These bounds were calculated at several values of ϕ_T and are plotted as dashed lines in Figure 12. The majority of the experimental data fall within these upper and lower bounds. This result quite strongly supports the model proposed for subgrain boundary intersections driving grain-boundary migration. However, approximately 20% of the data points do fall outside the predicted 95% bounds. These points may correspond to intersections that are not in a state of equilibrium, as it is unreasonable to expect that all intersections reached equilibrium prior to experimental observation.

VI. CONCLUSIONS

HR-EBSD data were successfully collected from Ti-IF steel specimens deformed in tension at $\dot{\epsilon} = 10^{-4}$ s^{-1} and 850 °C and were used to measure subgrain features formed during deformation. A model for dynamic grain growth (DGG) involving the intersections of subgrain boundaries with high-angle grain boundaries was tested against these data. The following conclusions are offered from this investigation.

1. Dynamic normal grain growth occurred in the Ti-IF steel material during tensile straining at $\dot{\epsilon} = 10^{-4}$ s^{-1} and 850 °C. Grain size increased approximately linearly with true strain during DGG. DGG was significantly faster than static grain growth (SGG) for similar exposure times at this temperature.
2. DGG increased the α-fiber and slightly decreased the γ-fiber texture components during tensile straining along the sheet rolling direction. No significant texture changes were observed from SGG.
3. DGG shifted grain size distributions to larger sizes but created pronounced left tails in those distributions. A long left tail suggests a population of small grains resistant to DGG. This is a characteristic feature of DGG that distinguishes it from SGG in the Ti-IF steel material.
4. HR-EBSD provided relative angular resolutions sufficient to identify subgrains, measure subgrain size, and measure the misorientations of individual subgrain boundaries.
5. The average subgrain size was approximately constant with plastic strain during steady-state flow, despite significant grain growth.
6. Subgrain boundary misorientations increased with increasing plastic strain, but the rate of increase slowed as true strain exceeded 0.1.
7. A model was proposed for DGG in which intersecting subgrain boundaries drive the migration of high-angle boundaries. By this model, the driving pressure for boundary migration from subgrain boundaries is approximately one order in magnitude greater than that from the elimination of dislocation density alone.
8. The proposed model for DGG predicts the formation of cusps in grain boundaries at intersections with subgrain boundaries. Experimental measurements of the dihedral angle ϕ at these cusps agree with predictions from theory.

ACKNOWLEDGMENTS

The authors thank the National Science Foundation for sponsoring this work under Grant DMR-2003312 and instrumentation under Grant DMR-9974476. This work was performed, in part, at the Center for Integrated Nanotechnologies, an Office of Science User Facility operated for the U.S. Department of Energy (DOE) Office of Science by Los Alamos National Laboratory (Contract 89233218CNA000001) and Sandia National Laboratories (Contract DE-NA-0003525). The authors are grateful to Mr. Toshiyasu Ukena (Nippon Steel, retired) for his suggestions and recommendations important to establishing and then

developing this research effort. Mr. Thomas Cayia (Arcelor Mittal) is gratefully acknowledged for providing the interstitial-free steel material used in this study.

CONFLICT OF INTEREST

The authors declare that they have no conflict of interest.

REFERENCES

1. J.G. Byrne: *Recovery, Recrystallization, and Grain Growth*, The Macmillan Company, New York, 1965.
2. M.A. Clark and T.H. Alden: *Acta Metall.*, 1973, vol. 21(9), pp. 1195–1206.
3. O.N. Senkov and M.M. Myshlyaev: *Acta Metall.*, 1986, vol. 34(1), pp. 97–106.
4. D.S. Wilkinson and C.H. Cáceres: *Acta Metall.*, 1984, vol. 32(9), pp. 1335–45.
5. M.K. Rabinovich and V.G. Trifonov: *Acta Mater.*, 1996, vol. 44(5), pp. 2073–78.
6. B.-N. Kim, K. Hiraga, Y. Sakka, and B.-W. Ahn: *Acta Mater.*, 1999, vol. 47(12), pp. 3433–39.
7. P.S. Bate, K.B. Hyde, S.A. Court, and F.J. Humphreys: *Mater. Sci. Forum.*, 2004, vol. 447-448, pp. 61–66.
8. K.B. Hyde and P.S. Bate: *Acta Mater.*, 2005, vol. 53(16), pp. 4313–21.
9. O.V. Rofman and P.S. Bate: *Acta Mater.*, 2010, vol. 58(7), pp. 2527–34.
10. J.R. Ciulik and E.M. Taleff: *Scr. Mater.*, 2009, vol. 61(10), pp. 895–98.
11. N.A. Pedrazas, T.E. Buchheit, E.A. Holm, and E.M. Taleff: *Mater. Sci. Eng., A*, 2013, vol. 610, pp. 76–84.
12. D.L. Worthington, N.A. Pedrazas, and P.J. Noell, E.M. Taleff: *Metall. Mater. Trans. A*, 2013, vol. 44(11), pp. 5025–38.
13. P.J. Noell and E.M. Taleff: *JOM*, 2015, vol. 67(11), pp. 2642–45.
14. P.J. Noell, D.L. Worthington, and E.M. Taleff: *Metall. Mater. Trans. A*, 2015, vol. 46(12), pp. 5709–18.
15. P.J. Noell and E.M. Taleff: *Metall. Mater. Trans. A*, 2016, vol. 47(10), pp. 5023–36.
16. P.J. Noell, D.L. Worthington, and E.M. Taleff: *Mater. Sci. Eng., A*, 2017, vol. 692, pp. 24–34.
17. P.J. Noell and E.M. Taleff: *Metall. Mater. Trans. A*, 2019, vol. 50A(10), pp. 4608–19.
18. R.E. Rupp, P.J. Noell, and E.M. Taleff: *Metall. Mater. Trans. A*, 2020, vol. 51A(12), pp. 6167–83.
19. J. Humphreys, G.S. Rohrer, and A. Rollet: *Recrystallization and Related Annealing Phenomena*, 3rd ed., Elsevier, Cambridge, MA, 2017.
20. G. Gottstein and L.S. Shvindlerman: *Grain Boundary Migration in Metals*, CRC Press, Boca Raton, FL, 2010.
21. A. Bhattacharya, Y.-F. Shen, C.M. Hefferan, S.F. Li, J. Lind, R.M. Suter, C.E. Krill, and G.S. Rohrer: *Science*, 2021, vol. 374(6564), pp. 189–93.
22. R.C. Gifkins: *Trans. Metall. Soc. AIME*, 1959, vol. 215, pp. 1015–22.
23. P.S. Bate: *Acta Mater.*, 2001, vol. 49(8), pp. 1453–61.
24. Y. Onuki, R. Hongo, K. Okayasu, and H. Fukutomi: *Acta Mater.*, 2013, vol. 61, pp. 1294–1302.
25. C.R. Barrett, W.D. Nix, and O.D. Sherby: *ASM Trans. Q.*, 1966, vol. 59(1), pp. 3–15.
26. O.D. Sherby and P.M. Burke: *Prog. Mater. Sci.*, 1968, vol. 13, pp. 325–90.
27. J.E. Bird, A.K. Mukherjee, and J.E. Dorn: in D.G. Brandon and A. Rosen, eds., *Proceedings of the International Conference on Quantitative Relation Between Properties and Microstructure*, Israel Universities Press, Haifa, Israel, 1969, pp. 255–42.
28. S. Karashima, T. Iikubo, and H. Oikawa: *Trans. Jpn. Inst. Met.*, 1972, vol. 13(3), pp. 176–81.
29. S.F. Exell and D.H. Warrington: *Philos. Mag.*, 1972, vol. 26(5), pp. 1121–36.
30. R.G. Stang, W.D. Nix, and C.R. Barrett: *Metall. Trans. A*, 1975, vol. 6A, pp. 2065–17.
31. M.E. Kassner and M.E. McMahon: *Metall. Trans. A*, 1987, vol. 18(5), pp. 835–46.
32. A. Einstein: *Ann. Phys.*, 1905, vol. 322(8), pp. 549–60.
33. W. Sutherland: *Philos. Mag.*, 1905, vol. 9(54), pp. 781–85.
34. M. von Smoluchowski: *Ann. Phys.*, 1906, vol. 326(14), pp. 756–80.
35. M. Winning, G. Gottstein, and L.S. Shvindlerman: *Acta Mater.*, 2001, vol. 49(2), pp. 211–19.
36. M. Winning, G. Gottstein, and L.S. Shvindlerman: *Mater. Sci. Eng., A*, 2001, vol. 317(1–2), pp. 17–20.
37. J.W. Cahn and J.E. Taylor: *Acta Mater.*, 2004, vol. 52(16), pp. 4887–98.
38. J.W. Cahn, Y. Mishin, and A. Suzuku: *Acta Mater.*, 2006, vol. 54, pp. 4953–75.
39. J. Han, S.L. Thomas, and D.J. Srolovitz: *Prog. Mater. Sci.*, 2018, vol. 98, pp. 386–476.
40. J. Weertman and J.R. Weertman: *Elementary Dislocation Theory*, Macmillan, New York, 1964.
41. J.P. Hirth and J. Lothe: *Theory of Dislocations*, Wiley, New York, 2nd ed., 1982.
42. D. Hull and D.J. Bacon: *Introduction to Dislocations*, 5th ed., Elsevier/Butterworth-Hienemann, Burlington, MA, 2011.
43. W.R. Cannon and O.D. Sherby: *Metall. Trans.*, 1970, vol. 1(4), pp. 1030–32.
44. P. Yavari, F.A. Mohamed, and T.G. Langdon: *Acta Metall.*, 1981, vol. 29(8), pp. 1495–1507.
45. W. Shockley and W.T. Read: *Phys. Rev.*, 1949, vol. 75, pp. 692.
46. W.T. Read and W. Shockley: *Phys. Rev.*, 1950, vol. 78(3), pp. 275–89.
47. W. Köster: *Z. Metallkd.*, 1948, vol. 39, pp. 1–9.
48. T.J. Bennett, IV: Master's thesis, The University of Texas at Austin, 2022.
49. MTEX documentation, https://mtex-toolbox.github.io/Documentation.html, 2023.
50. MathWorks Inc.: Matlab, version R2022a, 2022.
51. R. Bergmann, R.H. Chan, R. Hielscher, J. Persch, and G. Steidl: *Inverse Prob. Imaging*, 2016, vol. 10(2), pp. 281–304.
52. S.A. Saltykov: *Stereometric Metallurgy*, vol. 2, 2nd ed., Armed Services Technical Information Agency, Arlington, VA, 1961.
53. ASTM International: *Standard Designation E112–13*, ASTM International, West Conshohocken, PA, 2013.
54. A.J. Wilkinson, G. Meaden, and D.J. Dingley: *Ultramicroscopy*, 2006, vol. 106(4), pp. 307–13.
55. OpenXY, https://github.com/BYU-MicrostructureOfMaterials/OpenXY, 2023.
56. G.I. Taylor: *J. Inst. Met.*, 1938, vol. 62(1), pp. 307–24.
57. D.N. Joanes and C.A. Gill: *J. R. Stat. Soc. Ser. D)*, 1998, vol. 47(1), pp. 183–89.
58. J. Lin and O.D. Sherby: *Res Mech.*, 1981, vol. 2(4), pp. 251–93.
59. O.D. Sherby, A.K. Miller, and M.E. Kassner: *Met. Forum*, 1981, vol. 4(1–2), pp. 53–56.
60. O.D. Sherby, R.H. Klundt, and A.K. Miller: *Metall. Trans. A*, 1977, vol. 8A(6), pp. 843–50.
61. S.O. Robinson, C.M. Young, and O.D. Sherby: *J. Mater. Sci.*, 1974, vol. 9(2), pp. 341–43.
62. C.M. Young and O.D. Sherby: *J. Iron Steel Inst., London*, 1973, vol. 211(9), pp. 640–47.
63. O.D. Sherby and J. Wadsworth: *Prog. Mater. Sci.*, 1989, vol. 33, pp. 169–221.
64. W.C. Lenthe, S. Singh, and M. De Graef: *Ultramicroscopy*, 2019, vol. 207, pp. 112841.
65. S. Singh, F. Ram, and M. De Graef: *Microsc. Microanal.*, 2017, vol. 23(S1), pp. 212–13.
66. S.F. Subramanian, M. Prikryl, B.D. Gaulin, D.D. Clifford, S. Benincasa, and I. O'Reilly: *ISIJ Int.*, 1994, vol. 34(1), pp. 61–69.
67. T.A. Roth: *Mater. Sci. Eng.*, 1975, vol. 18, pp. 183–92.
68. E.D. Hondros: *Proc. R. S. A*, 1965, vol. 286(1407), pp. 479–98.
69. A.T. Price, H. Holl, and A.P. Greenough: *Acta Metall.*, 1964, vol. 12(1), pp. 49–58.

70. L.E. Murr: *Interfacial Phenomena in Metals and Alloys*, Addison-Wesley Publishing Company, Reading, MA, 1975.
71. E.D. Hondros and L.E.H. Stuart: *Philos. Mag.*, 1968, vol. 17(148), pp. 711–27.
72. A. Jaatinen, C.V. Achim, K.R. Elder, and T. Ala-Nissila: *Technische Mechanik*, 2010, vol. 30(1–3), pp. 169–76.
73. S. Ratanaphan, D.L. Olmsted, V.V. Bulatov, E.A. Holm, A.D. Rollett, and G.S. Rohrer: *Acta Mater.*, 2015, vol. 88, pp. 346–54.
74. J. Wang, G.K.H. Madsen, and R. Drautz: Grain boundaries in BCC-Fe: *Modell. Simul. Mater. Sci. Eng.*, 2018, vol. 26, pp. 025008.
75. C.G. Dunn and F. Lionetti: *Trans. AIME*, 1949, vol. 1(2), pp. 125–32.
76. C.G. Dunn, F.W. Daniels, and M.J. Bolton: *Trans. AIME*, 1950, vol. 188, pp. 1245–48.
77. H.J. Frost and M.F. Ashby: *Deformation-Mechanism Maps, The Plasticity and Creep of Metals and Ceramics*, Pergamon Press Inc., New York, NY, 1982.
78. J.P. Butler and J.A. Reeds: *SIAM J. Appl. Math.*, 1987, vol. 47(3), pp. 670–77.
79. J.A. Reeds and J.P. Butler: *SIAM J. Appl. Math.*, 1987, vol. 47(3), pp. 678–87.
80. B.C. Carlson: *Numer. Math.*, 1979, vol. 33(1), pp. 1–16.
81. B.C. Carlson and E.M. Notis: *ACM Trans. Math. Software*, 1981, vol. 7(3), pp. 398–403.